Chapter 14

Near-to-Far-Field Transformation

14.1 Introduction

As we have seen, the FDTD method provides the fields throughout some finite region of space, i.e., the fields throughout the computational domain. However, in practice, we are often interested in the fields far away from the region we have modeled. For example, an FDTD implementation may have modeled an antenna or some scatterer. But, the fields in the immediate vicinity of that antenna or scatterer may not be the primary concern. Rather, the distant or "far" fields may be the primary concern. In this chapter we show how the near fields, which are essentially the fields within the FDTD grid, can be used to obtain the far fields. We start with a brief review of the underlying theory that pertains in the continuous world and then discuss the implementation details for the FDTD method.

14.2 The Equivalence Principle

Recall the boundary conditions that pertain to the electric and magnetic fields tangential to an interface:

$$\hat{\mathbf{n}}' \times (\mathbf{E}_1 - \mathbf{E}_2) = -\mathbf{M}_s, \tag{14.1}$$

$$\hat{\mathbf{n}}' \times (\mathbf{H}_1 - \mathbf{H}_2) = \mathbf{J}_s, \tag{14.2}$$

where $\hat{\mathbf{n}}'$ is normal to the interface, pointing toward region 1. The subscript 1 indicates the fields immediately adjacent to one side of the interface and the subscript 2 indicates the fields just on the other side of the interface. The "interface" can either be a physical boundary between two media or a fictitious boundary with the same medium to either side. The current $\mathbf{M}_s$ is a magnetic surface current, i.e., a current that only flows tangential to the interface. In practice there is no magnetic charge and thus no magnetic current. Therefore (14.1) states that the tangential components of $\mathbf{E}$ must be continuous across the boundary. However, in theory, we can imagine a scenario where the tangential fields are discontinuous. If this were the case, the magnetic current $\mathbf{M}_s$ must be non-zero to account for this discontinuity. In a little while we will see why it is convenient to envision such a scenario. The current $\mathbf{J}_s$ in (14.2) is the usual electric surface current.

As depicted in Fig. 14.1(a), consider a space in which there is a source or scatterer that radiates (or scatters) some fields. We can define a fictitious boundary that surrounds this source or scatterer. Let us then imagine that the fields exterior to this boundary are unchanged but the fields interior to the boundary are set to zero as depicted in Fig. 14.1(b). By setting the fields interior to the boundary to zero, we will create discontinuities in the tangential components on either side of the fictitious boundary. These discontinuities are perfectly fine provided we account for them by having the appropriate surface currents flow over the boundary. These currents are given by (14.1) and (14.2) where the fields in region 2 are now zero. Thus,

$$\mathbf{M}_s = -\hat{\mathbf{n}}' \times \mathbf{E}_1, \tag{14.3}$$

$$\mathbf{J}_s = \hat{\mathbf{n}}' \times \mathbf{H}_1. \tag{14.4}$$

As you may recall and as will be discussed in further detail below, it is fairly simple to find the fields radiated by a current (whether electric or magnetic) when that current is radiating in a homogeneous medium. Unfortunately, as shown in Fig. 14.1(b), the surface currents are not radiating in a homogeneous medium. But, in fact, since the fields within the fictitious boundary are zero, we can place anything, or nothing, within the boundary and that will have no effect on the fields exterior to the boundary. So, let us maintain the same surface currents but discard any inhomogeneity that were within the boundary. That leaves a homogeneous region as depicted in Fig. 14.1(c) and it is fairly straightforward to find these radiated fields.

14.3   Vector Potentials

Before proceeding further, let us briefly review vector potentials. First, consider the case (which corresponds to the physical world) where there is no magnetic charge—electric currents can flow but magnetic currents cannot. Thus,

$$\nabla \cdot \mathbf{B}_A = \nabla \cdot \mu \mathbf{H}_A = 0 \tag{14.5}$$

where the subscript A indicates we are considering the case of no magnetic charge. There is a vector identity that the divergence of the curl of any vector field is identically zero. Therefore (14.5) will automatically be satisfied if we write

$$\mathbf{H}_A = \frac{1}{\mu} \nabla \times \mathbf{A} \tag{14.6}$$

where $\mathbf{A}$ is a yet-to-be-determined field known as the magnetic vector potential. Now, using Faraday's law we obtain

$$\nabla \times \mathbf{E}_A = -j\omega\mu\mathbf{H}_A = -j\omega\nabla \times \mathbf{A}. \tag{14.7}$$

Using the terms on the left and the right and regrouping yields

$$\nabla \times (\mathbf{E}_A + j\omega\mathbf{A}) = 0. \tag{14.8}$$

The curl of the gradient of any function is identically zero. Thus we can set the term in parentheses equal to the (negative of the) gradient of some unknown scalar electric potential function Φ_e and in this way (14.8) will automatically be satisfied. Therefore we have

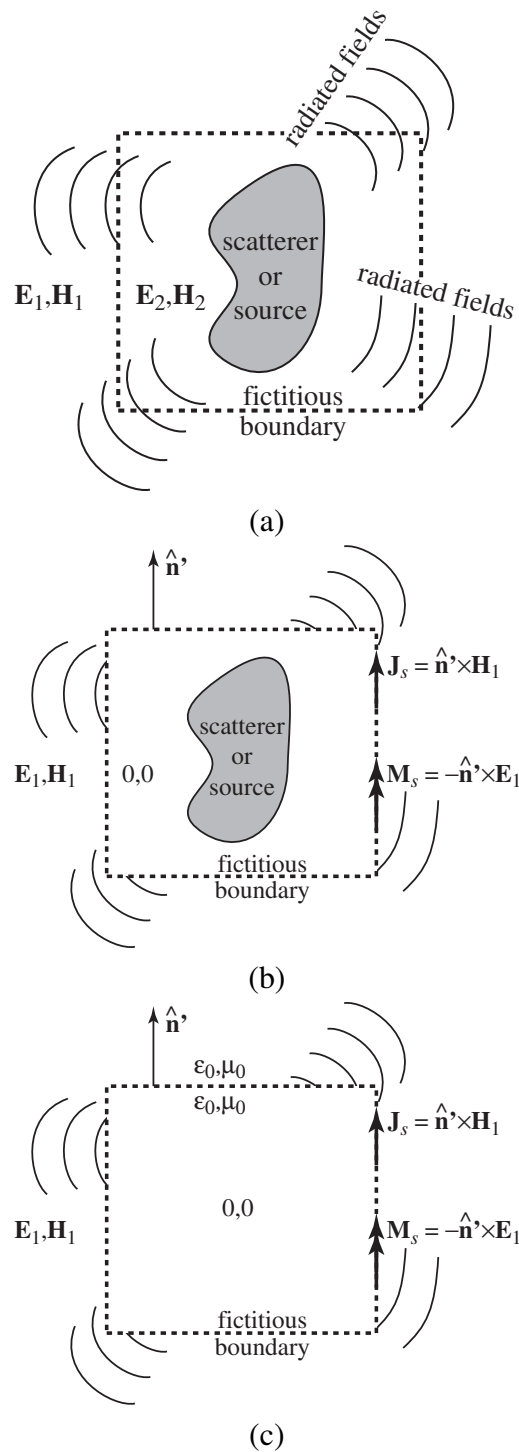$$\mathbf{E}_A + j\omega\mathbf{A} = -\nabla\Phi_e \tag{14.9}$$

Figure 14.1: (a) A space containing a source or scatterer that is surrounded by a fictitious boundary which is indicated by the dashed line. The fields are continuous across this boundary. (b) The fields are set to zero within the boundary. Surface currents must be used to account for the discontinuity across the boundary. (c) Since the fields are zero within the boundary, any inhomogeneities within the boundary can be discarded.

or, after rearranging,

$$\mathbf{E}_A = -j\omega\mathbf{A} - \nabla\Phi_e. \tag{14.10}$$

Using the remaining curl equation, Ampere's law, we can write

$$\nabla \times \mathbf{H}_A = \mathbf{J} + j\omega\epsilon\mathbf{E}_A \tag{14.11}$$

$$\nabla \times \frac{1}{\mu}\nabla \times \mathbf{A} = \mathbf{J} + j\omega\epsilon(-j\omega\mathbf{A} - \nabla\Phi_e) \tag{14.12}$$

Multiplying through by μ and expanding the curl operations yields

$$\nabla(\nabla \cdot \mathbf{A}) - \nabla^2\mathbf{A} = \mu\mathbf{J} + \omega^2\mu\epsilon\mathbf{A} - j\omega\mu\epsilon\nabla\Phi_e. \tag{14.13}$$

Regrouping terms yields

$$\nabla^2\mathbf{A} + \omega^2\mu\epsilon\mathbf{A} = -\mu\mathbf{J} + \nabla(\nabla \cdot \mathbf{A} + j\omega\mu\epsilon\Phi_e). \tag{14.14}$$

So far we have said what the curl of $\mathbf{A}$ must be, but that does not fully describe the field. To fully describe a vector field one must specify the curl, the divergence, and the value at a point (which we will ultimately assume is zero at a infinite distance from the origin). We are free to make the divergence of $\mathbf{A}$ any convenient value. Let us use the "Lorentz gauge" of

$$\nabla \cdot \mathbf{A} = -j\omega\mu\epsilon\Phi_e. \tag{14.15}$$

By doing this, (14.14) reduces to

$$\nabla^2\mathbf{A} + k^2\mathbf{A} = -\mu\mathbf{J}. \tag{14.16}$$

where $k = \omega\sqrt{\mu\epsilon}$.

Distinct from the scenario described above, let us imagine a situation where there is no free electric charge. Magnetic currents can flow, but electric currents cannot. Thus the divergence of the electric flux density is

$$\nabla \cdot \mathbf{D}_F = \nabla \cdot \epsilon\mathbf{E}_F = 0 \tag{14.17}$$

where here the subscript F is used to indicate the case of no electric charge. Again, this equation will be satisfied automatically if we represent the electric field as the curl of some potential function $\mathbf{F}$. To this end we write

$$\mathbf{E}_F = -\frac{1}{\epsilon}\nabla \times \mathbf{F} \tag{14.18}$$

where $\mathbf{F}$ is known as the electric vector potential.

Following steps similar to the ones we used to obtain (14.16), one can obtain the differential equation that governs $\mathbf{F}$, namely,

$$\nabla^2\mathbf{F} + k^2\mathbf{F} = -\epsilon\mathbf{M}. \tag{14.19}$$

Thus both $\mathbf{A}$ and $\mathbf{F}$ are governed by the wave equation. We see that the source of $\mathbf{A}$, i.e., the forcing function that creates $\mathbf{A}$ is the electric current $\mathbf{J}$. Similarly, the source of $\mathbf{F}$ is the magnetic current $\mathbf{M}$. (We have not yet restricted these currents to be surface currents. At this point they can be any current distribution, whether distributed throughout a volume, over a surface, or along a line.)

Note that both the Laplacian (∇^2) and the constant k^2 that appear in (14.16) and (14.19) are scalar operators. They do not change the orientation of a vector. Thus, the x component of $\mathbf{J}$ gives

rise to the x component of $\mathbf{A}$, the y component of $\mathbf{M}$ gives rise to the y component of $\mathbf{F}$, and so on. In this way, (14.16) and (14.19) could each be broken into their three Cartesian components and we would be left with six scalar equations.

These equations have relatively straightforward solutions. Let us consider a slightly simplified problem, the solution of which can easily be extended to the full general problem. Consider the case of an incremental current of length $d\ell$ that is located at the origin and oriented in the z direction. In this case (14.16) reduces to

$$\nabla^2 A_z(\mathbf{r}) + k^2 A_z(\mathbf{r}) = -\mu I d\ell \delta(\mathbf{r}) \tag{14.20}$$

where I is the amount of current and $\delta(\mathbf{r})$ is the 3D Dirac delta function. The Dirac delta function is zero expect when its argument is zero. For an argument of zero, $\delta(\mathbf{r})$ is singular, i.e., infinite. However, this singularity is integrable. A volume integral of any region of space that includes the Dirac delta function at the origin (i.e., $\mathbf{r} = 0$) will yield unit volume. For any observation point other than the origin, (14.20) can be written

$$\nabla^2 A_z(\mathbf{r}) + k^2 A_z(\mathbf{r}) = 0 \qquad \mathbf{r} \neq 0. \tag{14.21}$$

It is rather easy to show that a general solution to this is

$$A_z(\mathbf{r}) = C_1 \frac{e^{-jkr}}{r} + C_2 \frac{e^{jkr}}{r}. \tag{14.22}$$

We discard the second term on the right-hand side since that represents a spherical wave propagating in toward the origin. Thus we are left with

$$A_z(\mathbf{r}) = C_1 \frac{e^{-jkr}}{r} \tag{14.23}$$

where we must now determine the constant C_1 based on the "driving function" on the right side of (14.20).

To obtain C_1, we integrate both side of (14.20) over a small spherical volume of radius r_0 and take the limit as r_0 approaches zero:

$$\lim_{r_0 \to 0} \int_V \left[\nabla^2 A_z + k^2 A_z\right] dv = \lim_{r_0 \to 0} \int_V -\mu I d\ell \delta(\mathbf{r}) dv. \tag{14.24}$$

Using the sifting property of the delta function, the right-hand side of (14.24) is simply $-\mu I d\ell$. For the left-hand side, we first expand the integral associated with the second term in the square brackets

$$\lim_{r_0 \to 0} \int_{r=0}^{r_0} \int_{\theta=0}^{\pi} \int_{\phi=0}^{2\pi} k^2 C_1 \frac{e^{-jkr}}{r} r^2 \sin\theta \, d\phi \, d\theta \, dr. \tag{14.25}$$

Including the term $r^2 \sin\theta$, which is contributed by the volume element dv, the entire integrand is proportional to r. Therefore as r_0 (the upper limit of integration in r) goes to zero, this integral goes to zero.

The remaining integral on the left side of (14.24) is

$$\lim_{r_0 \to 0} \int_V \nabla \cdot \nabla A_z dv = \lim_{r_0 \to 0} \oint_S \nabla A_z \cdot \mathbf{ds} \tag{14.26}$$

where we have used the divergence theorem to convert the volume integral to a surface integral (and used the fact that $\nabla^2 = \nabla \cdot \nabla$). The integrand of the surface integral is given by

$$\nabla A_z|_{r=r_0} = \hat{r} \frac{\partial A_z}{\partial r}\bigg|_{r=r_0} = \hat{r} \left(-\frac{e^{-jkr_0}}{r_0^2} - jk\frac{e^{-jkr_0}}{r_0} \right) C_1. \tag{14.27}$$

The surface element $\mathbf{ds}$ is given by $\hat{r} \, r_0^2 \sin\theta d\phi \, d\theta$ so that the entire surface integral is given by

$$\lim_{r_0 \to 0} \int_{\theta=0}^{\pi} \int_{\phi=0}^{2\pi} C_1 e^{-jkr_0}(-1 - jkr_0)\sin\theta d\phi \, d\theta = \lim_{r_0 \to 0} -C_1 e^{-jkr_0}(1 + jkr_0)4\pi = -C_1 4\pi. \tag{14.28}$$

Equating this with the right-hand side of (14.20), we can solve for C_1. The final result is

$$C_1 = \frac{\mu I d\ell}{4\pi}. \tag{14.29}$$

It should be noted that there is actually nothing special about having r_0 approach zero. The same coefficient is obtained for any value of r_0. Letting r_0 approach zero merely simplifies the problem a bit.

We now have that a filamentary current I of length $d\ell$ located at the origin and oriented in the z direction produces the vector potential

$$A_z(\mathbf{r}) = \frac{\mu I d\ell}{4\pi} \frac{e^{-jkr}}{r}. \tag{14.30}$$

This is simply a spherical wave radiating symmetrically away from the origin. If the source is located at the point $\mathbf{r}'$ instead of the origin, one merely needs to account for this displacement. The vector potential in that case is

$$A_z(\mathbf{r}) = \frac{\mu I d\ell}{4\pi} \frac{e^{-jk|\mathbf{r}-\mathbf{r}'|}}{|\mathbf{r} - \mathbf{r}'|}. \tag{14.31}$$

If the current was oriented in the x or y direction, that would produce a vector potential that only had a x or y component, respectively.

For a current source, the "strength" of the source is, in one way of thinking, determined by the amount of current that is flowing times the length over which that current flows. For a filament we have that the "source strength" is given by $I d\ell$. For a surface current the equivalent concept is $J_s ds$ where J_s is the surface current density in Amperes/meter and ds is an incremental surface area. Similarly, for a volumetric current, the equivalent term is $J dv$ where J is the current density in Amperes/meter^2 and dv is an incremental volume.

Instead of having just a point source, currents can be distributed throughout space. To get the corresponding vector potentials, we merely have to sum the contributions of the current wherever it

exists, accounting for the location (displacement from the origin), the orientation, and the amount of current.

For surface currents, the vector potentials are given by

$$\mathbf{A}(\mathbf{r}) \;=\; \mu \oint_S \mathbf{J}_s(\mathbf{r}')\frac{e^{-jk|\mathbf{r}-\mathbf{r}'|}}{4\pi|\mathbf{r}-\mathbf{r}'|}ds', \tag{14.32}$$

$$\mathbf{F}(\mathbf{r}) \;=\; \epsilon \oint_S \mathbf{M}_s(\mathbf{r}')\frac{e^{-jk|\mathbf{r}-\mathbf{r}'|}}{4\pi|\mathbf{r}-\mathbf{r}'|}ds', \tag{14.33}$$

where, as before, $\mathbf{r}$ is the observation point, $\mathbf{r}'$ is the location of the source point (i.e., the location of the currents), and S is the surface over which the current flows.

Equations (14.32) and (14.33) give the vector potentials at an arbitrary observation point $\mathbf{r}$ in three dimensions. The surface S is a surface that exists in the 3D space (such as the surface of sphere or a cube).

Let us consider the two-dimensional case. We can consider the 2D case as a special case in 3D in which there is no variation in the z direction. The observation point is a point in the xy plane specified by the vector $\boldsymbol{\rho}$. Thus, the magnetic vector potential could be written as

$$\mathbf{A}(\boldsymbol{\rho}) \;=\; \mu \oint_L \int_{z'=-\infty}^{\infty} \mathbf{J}_s(\boldsymbol{\rho}')\frac{e^{-jk\sqrt{|\boldsymbol{\rho}-\boldsymbol{\rho}'|^2+z'^2}}}{4\pi\sqrt{|\boldsymbol{\rho}-\boldsymbol{\rho}'|^2+z'^2}}dz'd\ell', \tag{14.34}$$

$$=\; \mu \oint_L \mathbf{J}_s(\boldsymbol{\rho}')\left(\int_{z'=-\infty}^{\infty}\frac{e^{-jk\sqrt{|\boldsymbol{\rho}-\boldsymbol{\rho}'|^2+z'^2}}}{4\pi\sqrt{|\boldsymbol{\rho}-\boldsymbol{\rho}'|^2+z'^2}}dz'\right)d\ell'. \tag{14.35}$$

The term in parentheses can be integrated to obtain

$$\int_{z'=-\infty}^{\infty}\frac{e^{-jk\sqrt{|\boldsymbol{\rho}-\boldsymbol{\rho}'|^2+z'^2}}}{4\pi\sqrt{|\boldsymbol{\rho}-\boldsymbol{\rho}'|^2+z'^2}}dz' = -\frac{j}{4}H_0^{(2)}(k|\boldsymbol{\rho}-\boldsymbol{\rho}'|) \tag{14.36}$$

where $H_0^{(2)}$ is the zeroth-order Hankel function of the second kind. This represents a cylindrical wave radiating from the point $\boldsymbol{\rho}'$. Similar steps can be done for $\mathbf{F}$ and in this way z is eliminated from the expressions for the vector potentials. We are left with a 2D representation of the fields, namely,

$$\mathbf{A}(\boldsymbol{\rho}) \;=\; -j\frac{\mu}{4}\oint_L \mathbf{J}(\boldsymbol{\rho}')H_0^{(2)}(k|\boldsymbol{\rho}-\boldsymbol{\rho}'|)d\ell', \tag{14.37}$$

$$\mathbf{F}(\boldsymbol{\rho}) \;=\; -j\frac{\epsilon}{4}\oint_L \mathbf{M}(\boldsymbol{\rho}')H_0^{(2)}(k|\boldsymbol{\rho}-\boldsymbol{\rho}'|)d\ell'. \tag{14.38}$$

where the explicit s subscript has been dropped from the currents.

The approximation of the zeroth-order Hankel function of the second kind as the argument ξ gets large is

$$H_0^{(2)}(k\xi) \approx \sqrt{\frac{j2}{\pi k\xi}}e^{-jk\xi}. \tag{14.39}$$

Now let $\xi = |\boldsymbol{\rho} - \boldsymbol{\rho}'|$ where ρ is large enough that the following approximations are valid:

$$\xi \approx \begin{cases} \rho - \rho' \cos\psi & \text{for the phase,} \\ \rho & \text{for the magnitude.} \end{cases} \tag{14.40}$$

where, referring to Fig. 14.2, ψ is the angle between the observation angle and the angle to the source point. (Because we are taking the cosine of ψ, and cosine is an even function, it doesn't matter if we define ψ as $\phi - \phi'$ or $\phi' - \phi$ but we will take ψ to be $\phi - \phi'$.) Thus the Hankel function can be written

$$H_0^{(2)}(k|\boldsymbol{\rho} - \boldsymbol{\rho}'|) \approx \sqrt{\frac{j2}{\pi k \rho}} e^{-jk\rho} e^{jk\rho' \cos\psi}. \tag{14.41}$$

The **A** vector potential for a 2D problem can thus be written

$$\mathbf{A}(\boldsymbol{\rho}) = -j\frac{\mu}{4} \oint_L \mathbf{J}(\boldsymbol{\rho}') H_0^{(2)}(k|\boldsymbol{\rho} - \boldsymbol{\rho}'|) d\ell', \tag{14.42}$$

$$\approx -j\frac{\mu}{4} \sqrt{\frac{j2}{\pi k \rho}} e^{-jk\rho} \oint_L \mathbf{J}(\boldsymbol{\rho}') e^{jk\rho' \cos\psi} d\ell', \tag{14.43}$$

$$= -j\frac{\mu}{4} \sqrt{\frac{j2}{\pi k \rho}} e^{-jk\rho} \mathbf{N}_{2D}, \tag{14.44}$$

where

$$\mathbf{N}_{2D} = \oint_L \mathbf{J}(\boldsymbol{\rho}') e^{jk\rho' \cos\psi} d\ell'. \tag{14.45}$$

Correspondingly, the **F** vector potential can be written

$$\mathbf{F}(\boldsymbol{\rho}) = -j\frac{\epsilon}{4} \oint_L \mathbf{M}(\boldsymbol{\rho}') H_0^{(2)}(k|\boldsymbol{\rho} - \boldsymbol{\rho}'|) d\ell', \tag{14.46}$$

$$\approx -j\frac{\epsilon}{4} \sqrt{\frac{j2}{\pi k \rho}} e^{-jk\rho} \oint_L \mathbf{M}(\boldsymbol{\rho}') e^{jk\rho' \cos\psi} d\ell', \tag{14.47}$$

$$= -j\frac{\epsilon}{4} \sqrt{\frac{j2}{\pi k \rho}} e^{-jk\rho} \mathbf{L}_{2D}, \tag{14.48}$$

where

$$\mathbf{L}_{2D} = \oint_L \mathbf{M}(\boldsymbol{\rho}') e^{jk\rho' \cos\psi} d\ell'. \tag{14.49}$$

Nominally $\mathbf{N}_{2D}$ and $\mathbf{L}_{2D}$ are functions of $\boldsymbol{\rho}$. However, within these functions the only thing that depends on $\boldsymbol{\rho}$ is ψ. The angle ψ only changes for large changes in $\boldsymbol{\rho}$—incremental changes of $\boldsymbol{\rho}$ will not affect ψ. Thus, derivatives of $\mathbf{N}_{2D}$ or $\mathbf{L}_{2D}$ with respect to ρ, ϕ, or z (i.e., derivatives with respect to the unprimed coordinates) are zero. The geometry is depicted in Fig. 14.2.
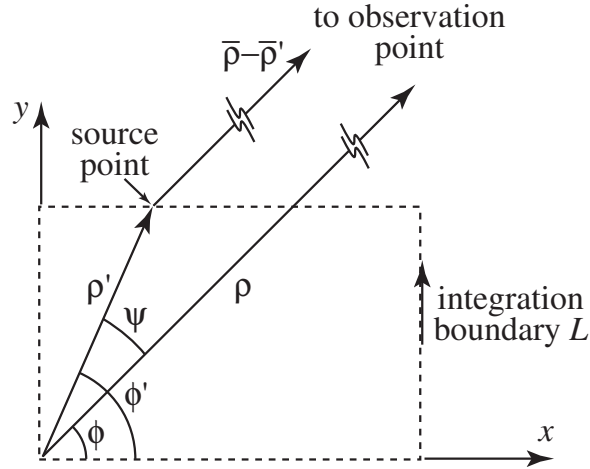
Figure 14.2: Geometry associated with the near-to-far-field transformation in 2D.

It is convenient to think of the currents, and subsequently $\mathbf{N}_{2D}$ and $\mathbf{L}_{2D}$ (and ultimately the potentials), in terms of cylindrical coordinates, i.e.,

$$
\begin{align}
\mathbf{J}(\boldsymbol{\rho}) &= J_\rho \hat{\mathbf{a}}_\rho + J_\phi \hat{\mathbf{a}}_\phi + J_z \hat{\mathbf{a}}_z, \tag{14.50} \\
\mathbf{M}(\boldsymbol{\rho}) &= M_\rho \hat{\mathbf{a}}_\rho + M_\phi \hat{\mathbf{a}}_\phi + M_z \hat{\mathbf{a}}_z. \tag{14.51}
\end{align}
$$

Combining the contributions from both $\mathbf{A}$ and $\mathbf{F}$, the electric and magnetic fields are given by

$$
\mathbf{E}(\boldsymbol{\rho}) = -j\omega \left[\mathbf{A} + \frac{1}{k^2}\nabla(\nabla \cdot \mathbf{A}) \right] - \frac{1}{\epsilon}\nabla \times \mathbf{F}, \tag{14.52}
$$

$$
\mathbf{H}(\boldsymbol{\rho}) = -j\omega \left[\mathbf{F} + \frac{1}{k^2}\nabla(\nabla \cdot \mathbf{F}) \right] + \frac{1}{\mu}\nabla \times \mathbf{A}. \tag{14.53}
$$

By plugging (14.44) and (14.48) into (14.52) and (14.53) and performing the various operations in cylindrical coordinates and discarding any terms that fall off faster than $1/\sqrt{\rho}$, one can obtain expressions for the electric and magnetic fields in the far field. (Note that the ∇ operator acts on the unprimed coordinates and, as mentioned above, $\mathbf{N}_{2D}$ and $\mathbf{L}_{2D}$ are not considered functions of the unprimed coordinates.)

14.4 Electric Field in the Far-Field

Following the steps outlined in the previous section, the scattered electric field $\mathbf{E}^s$ at the far-field point $\boldsymbol{\rho}$ can be obtained from the scattered "near" fields using

$$
\mathbf{E}^s(\boldsymbol{\rho}) = \sqrt{\frac{j}{8\pi k}} \frac{e^{-jk\rho}}{\sqrt{\rho}} \left\{ \hat{\mathbf{a}}_\phi \left(\omega\mu_0 \mathbf{N}_{2D} \cdot \hat{\mathbf{a}}_\phi + k\mathbf{L}_{2D} \cdot \hat{\mathbf{a}}_z \right) - \hat{\mathbf{a}}_z \left(\omega\mu_0 \mathbf{N}_{2D} \cdot \hat{\mathbf{a}}_z - k\mathbf{L}_{2D} \cdot \hat{\mathbf{a}}_\phi \right) \right\},
$$

$$
\tag{14.54}
$$

where, as stated previously,

$$\mathbf{N}_{\mathrm{2D}} = \oint_L \mathbf{J}(\boldsymbol{\rho}')e^{jk\rho'\cos\psi}d\ell', \tag{14.55}$$

$$\mathbf{L}_{\mathrm{2D}} = \oint_L \mathbf{M}(\boldsymbol{\rho}')e^{jk\rho'\cos\psi}d\ell', \tag{14.56}$$

L is the closed path of integration, ψ, given by $\phi - \phi'$, is the angle between the source point and observation point, $\mathbf{M} = -\hat{\mathbf{n}}' \times \mathbf{E}$, $\mathbf{J} = \hat{\mathbf{n}}' \times \mathbf{H}$, and $\hat{\mathbf{n}}'$ is a unit vector normal to the integration contour on the same side of the contour as the observation point (i.e., the outward normal). Unprimed coordinates correspond to the observation point while primed coordinates indicate the "source" location (i.e., points along the contour).

Let us now restrict consideration to TM^z polarization where the non-zero field are H_x, H_y, and E_z. Since the outward normal is restricted to exist in the xy plane, $\hat{\mathbf{n}}' \times \mathbf{H}$ only has a non-zero component in the z direction while $-\hat{\mathbf{n}}' \times \mathbf{E}$ only has non-zero components in the xy plane. Thus, for this polarization only the z component of the electric field is non-zero—the ϕ component of (14.54) is zero. The electric field can be written

$$E_z^s(\boldsymbol{\rho}) = -\sqrt{\frac{j}{8\pi k}}\frac{e^{-jk\rho}}{\sqrt{\rho}}\oint_L \left(\omega\mu_0\mathbf{J}(\boldsymbol{\rho}')\cdot\hat{\mathbf{a}}_z - k\mathbf{M}(\boldsymbol{\rho}')\cdot\hat{\mathbf{a}}_\phi\right)e^{jk\rho'\cos\psi}d\ell'. \tag{14.57}$$

Usually the scattering width is of more interest than the field itself. For TM^z polarization the two-dimensional scattering width is defined to be

$$\sigma_{\mathrm{2D}}(\phi) = \lim_{|\boldsymbol{\rho}-\boldsymbol{\rho}'|\to\infty} 2\pi\rho\frac{|E_z^s(\boldsymbol{\rho})|^2}{|E_z^i|^2} \tag{14.58}$$

Noting that $\omega\mu_0 = k\eta_0$ and plugging (14.57) into (14.58) and normalizing by the wavelength yields

$$\frac{\sigma_{\mathrm{2D}}(\phi)}{\lambda} = \frac{1}{8\pi|E_z^i|^2}\left|\oint_L \{\eta_0\mathbf{J}(\boldsymbol{\rho}')\cdot\hat{\mathbf{a}}_z - \mathbf{M}(\boldsymbol{\rho}')\cdot\hat{\mathbf{a}}_\phi\}e^{jkr'\cos(\phi-\phi')}kd\ell'\right|^2. \tag{14.59}$$

The term $r'\cos(\phi-\phi')$ which appears in the exponent can be written as $\hat{\mathbf{a}}_\rho\cdot\boldsymbol{\rho} = \hat{\mathbf{a}}_\rho\cdot(x'\hat{\mathbf{a}}_x+y'\hat{\mathbf{a}}_y) = x'\cos\phi + y'\sin\phi$. This last form is especially useful since ϕ is fixed by the observation direction and therefore the sine and cosine functions can be determined outside of any loop (rather than over and over again as we move along the integration contour).

For TM^z polarization the unit vector normal to the integration path is restricted to lie in the xy plane, i.e., $\hat{\mathbf{n}}' = n_x'\hat{\mathbf{a}}_x + n_y'\hat{\mathbf{a}}_y$ where $(n_x'^2 + n_y'^2)^{1/2} = 1$. Thus, the electric current $\mathbf{J}$ is given by

$$\mathbf{J} = \hat{\mathbf{n}}' \times \mathbf{H} = \begin{vmatrix} \hat{\mathbf{a}}_x & \hat{\mathbf{a}}_y & \hat{\mathbf{a}}_z \\ n_x' & n_y' & 0 \\ H_x & H_y & 0 \end{vmatrix} = \hat{\mathbf{a}}_z(n_x'H_y - n_y'H_x). \tag{14.60}$$

The dot product of $\hat{\mathbf{a}}_z$ and $\mathbf{J}$ yields

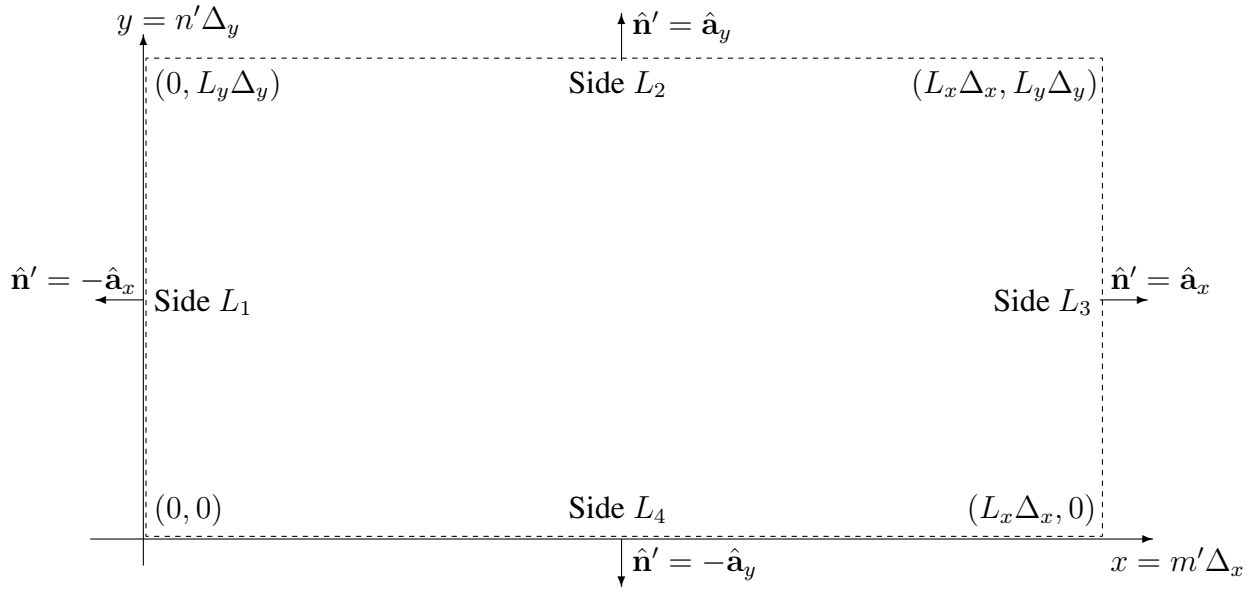$$\mathbf{J} \cdot \hat{\mathbf{a}}_z = n_x'H_y - n_y'H_x. \tag{14.61}$$

Figure 14.3: Depiction of integration boundary for near-to-far-field transformation in the FDTD grid.

The magnetic current is given by

$$\mathbf{M} = -\hat{\mathbf{n}}' \times \mathbf{E} = \begin{vmatrix} \hat{\mathbf{a}}_x & \hat{\mathbf{a}}_y & \hat{\mathbf{a}}_z \\ n'_x & n'_y & 0 \\ 0 & 0 & E_z \end{vmatrix} = -(\hat{\mathbf{a}}_x n'_y E_z - \hat{\mathbf{a}}_y n'_x E_z) \tag{14.62}$$

The dot product of $\hat{\mathbf{a}}_\phi$ and $\mathbf{M}$ yields

$$\mathbf{M} \cdot \hat{\mathbf{a}}_\phi = -\hat{\mathbf{a}}_x \cdot \hat{\mathbf{a}}_\phi n'_y E_z + \hat{\mathbf{a}}_y \cdot \hat{\mathbf{a}}_\phi n'_x E_z = (n'_y \sin \phi + n'_x \cos \phi) E_z \tag{14.63}$$

Incorporating (14.61) and (14.63) into (14.59) yields a general expression for the scattering width:

$$\frac{\sigma_{2D}(\phi)}{\lambda} = \frac{1}{8\pi |E^i_z|^2} \left| \oint_L \left\{ \eta_0 (n'_x H_y - n'_y H_x) - (n'_y \sin \phi + n'_x \cos \phi) E_z \right\} e^{jkr' \cos(\phi - \phi')} k d\ell' \right|^2. \tag{14.64}$$

We now want to specialize this equation to a rectangular box which is typical of the integration boundary which would be employed in an FDTD simulation.

Assume the integration boundary corresponds to the dashed box shown in Fig. 14.3. The width of this rectangle is $L_x \Delta_x$ and the height is $L_y \Delta_y$. In an FDTD grid there are $L_x + 1$ samples of the fields along the top and bottom (i.e., spanning the width) and $L_y + 1$ total samples along the left and right (i.e., spanning the height). The integration over the closed path L consists of the integration over the four sides of this box, i.e., $L = L_1 + L_2 + L_3 + L_4$. Using this geometry, the quantities needed to perform each integral are presented in the following two tables.

	$\hat{\mathbf{n}}'$		$\mathbf{J} \cdot \hat{\mathbf{a}}_z$	$\mathbf{M} \cdot \hat{\mathbf{a}}_\phi$
Side L_1	$n'_x = -1$	$n'_y = 0$	$-H_y$	$-\cos\phi E_z$
Side L_2	$n'_x = 0$	$n'_y = 1$	$-H_x$	$\sin\phi E_z$
Side L_3	$n'_x = 1$	$n'_y = 0$	H_y	$\cos\phi E_z$
Side L_4	$n'_x = 0$	$n'_y = -1$	H_x	$-\sin\phi E_z$

	ϕ'	ρ'	$\hat{\mathbf{a}}_\rho \cdot \boldsymbol{\rho}'$
Side L_1	$\pi/2$	$n'\Delta_y$	$n'\Delta_y \sin\phi$
Side L_2	$\tan^{-1}(L_y/m')$	$\sqrt{(m'\Delta_x)^2 + (L_y\Delta_y)^2}$	$m'\Delta_x \cos\phi + L_y\Delta_y \sin\phi$
Side L_3	$\tan^{-1}(n'/L_x)$	$\sqrt{(L_x\Delta_x)^2 + (n'\Delta_y)^2}$	$L_x\Delta_x \cos\phi + n'\Delta_y \sin\phi$
Side L_4	0	$m'\Delta_x \cos\phi$	$m'\Delta_y$

Note that in the second table the value n' represents the vertical displacement along Side L_1 or L_3. It varies between 0 and L_y and should not be confused with the outward normal $\hat{\mathbf{n}}'$ and its components n'_x and n'_y.

Assume that the spatial step sizes are equal so that $\Delta_x = \Delta_y = \delta$. Further assume that the problem has be discretized using N_λ points per wavelength so that the wavenumber can be written $k = 2\pi/\lambda = 2\pi/(N_\lambda \delta)$. Combining all together, the scattering width is given by

$$
\begin{aligned}
\frac{\sigma_{\text{2D}}(\phi)}{\lambda} \; = \; & \frac{1}{8\pi|E_z^i|^2} \left| \int_{m'=0}^{L_x} \left\{ [\eta_0 H_x(m',0) + \sin\phi E_z(m',0)] \, e^{j\frac{2\pi}{N_\lambda}m'\cos\phi} \right. \right. \\
& \left. - [\eta_0 H_x(m',L_y) + \sin\phi E_z(m',L_y)] \, e^{j\frac{2\pi}{N_\lambda}(m'\cos\phi + L_y\sin\phi)} \right\} \frac{2\pi}{N_\lambda} dm' \\
& + \int_{n'=0}^{L_y} \left\{ -[\eta_0 H_y(0,n') - \cos\phi E_z(0,n')] \, e^{j\frac{2\pi}{N_\lambda}n'\sin\phi} \right. \\
& \left. \left. + [\eta_0 H_y(L_x,n') - \cos\phi E_z(L_x,n')] \, e^{j\frac{2\pi}{N_\lambda}(L_x\cos\phi + n'\sin\phi)} \right\} \frac{2\pi}{N_\lambda} dn' \right|^2 \quad (14.65)
\end{aligned}
$$

Again we note that the integration variable for the second integral is n' which corresponds to displacement along the vertical sides. The fields in this expression are phasor (frequency-domain) quantities and hence are complex. Although this equation may look rather messy, as described in the next two sections, the phasors can be obtained rather simply with a running DFT and the integration can be calculated with a sum.

Because of the staggered nature of the FDTD grid, the electric and magnetic fields will not be collocated on the integration boundary—they will be offset in both space and time. A spatial average of either the electric or magnetic field will have to be performed to obtain the fields at the proper location. In the past, a simple arithmetic average was typically used to account for the spatial offsets. However, as will discussed, one can do better by using a harmonic average in space. For the temporal offset, a simple phase correction can be used to collocate the fields in time.
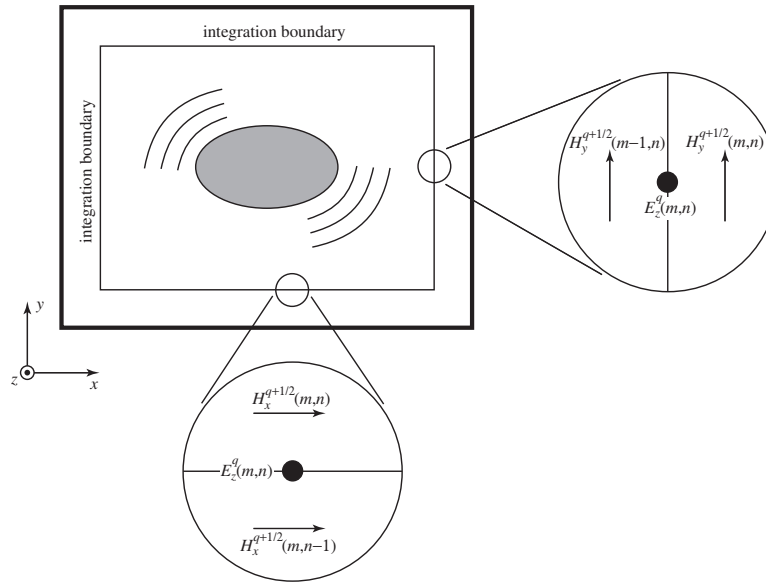
Figure 14.4: Depiction of a TM^z grid showing the integration boundary. The boundary is assumed to be aligned with electric-field nodes. The expanded views show the offset of the magnetic-field nodes from the boundary.

14.5 Simpson's Composite Integration

Assume we wish to integrate the function $f(x)$ over the interval $0 \leq x \leq L$ where L is an even integer. The integral can be obtained using Simpson's composite integration as follows

$$\int\limits_0^L f(x)dx \approx \frac{1}{3}\left[f(0) + 2\sum_{m=1}^{L/2-1} f(2m) + 4\sum_{m=1}^{L/2} f(2m-1) + f(L) \right] \tag{14.66}$$

Note that this approximation requires a total of $L + 1$ samples of the function (so we need an odd number of samples). Using Simpson's approximation yields quite a bit of additional accuracy over what would be obtained using a straight Riemann sum and it costs essentially nothing (it just requires slightly more bookkeeping).

14.6 Collocating the Electric and Magnetic Fields: The Geometric Mean

Figure 14.4 depicts an integration boundary in a TM^z grid. The boundary is assumed to be aligned with the electric-field nodes, i.e., the E_z nodes. The expanded views show a portion of the boundary along the right side and the bottom. The field notation employs superscripts to indicate time steps while spatial indices are given as arguments within parentheses. Half-step spatial offsets

are implicitly understood. Thus, the nodes in space-time and the corresponding notation are

$$
\begin{align}
H_x^{(q-1/2)\Delta_t}(m\Delta_x, [n+1/2]\Delta_y) &= H_x^{q-1/2}(m,n), \tag{14.67}\\
H_y^{(q-1/2)\Delta_t}([m+1/2]\Delta_x, n\Delta_y) &= H_y^{q-1/2}(m,n), \tag{14.68}\\
E_z^{q\Delta_t}(m\Delta_x, n\Delta_y) &= E_z^q(m,n), \tag{14.69}
\end{align}
$$

where Δ_x and Δ_y are the spatial steps in the x and y directions, respectively, and Δ_t is the temporal step. The index q indicates the temporal step and we assume it varies between 1 and N_T which is the total number of time-steps.

Near-to-far-field (NTFF) transforms require that the fields be defined over a single surface and use the same phase reference. For harmonic fields, the temporal offset can be easily accounted for with a phase factor. Assume the magnetic fields have been recorded at times of $q = 1/2, 3/2, 5/2, \ldots$ while the electric field has been recorded at times of $q = 1, 2, 3, \ldots$ For the harmonic transforms of interest here, the time-domain near-fields are Fourier transformed to the frequency domain. For example, the harmonic electric field on the boundary is given by

$$
\begin{align}
\hat{E}_z^k(m,n) &= \mathcal{F}\left[E_z^q(m,n)\right], \tag{14.70}\\
&= \frac{1}{N_T} \sum_{q=\langle N_T \rangle} E_z^q(m,n)e^{-jk\frac{2\pi}{N_T}q}. \tag{14.71}
\end{align}
$$

where $\mathcal{F}$ is the discrete Fourier transform. For situations where the entire spectrum is not of interest, typically a running discrete Fourier transform will be used only at the particular frequencies of interest. A frequency is specified by the index k which varies between zero (dc) and $N_T - 1$. Regardless of the implementation used, the resulting spectral terms $\hat{E}_z^k$ will be the same.

The time-domain series $E_z^q(m,n)$ can be obtained from $\hat{E}_z^k(m,n)$ via

$$
E_z^q(m,n) = \sum_{k=\langle N_T \rangle} \hat{E}_z^k(m,n)e^{jk\frac{2\pi}{N_T}q}. \tag{14.72}
$$

Because of the temporal offset between the electric and magnetic fields, the desired field is actually $E_z^{q-1/2}(m,n)$, thus, plugging $q - 1/2$ into (14.72) yields

$$
E_z^{q-1/2}(m,n) = \sum_{k=\langle N_T \rangle} \left(\hat{E}_z^k(m,n)e^{-jk\frac{\pi}{N_T}}\right) e^{jk\frac{2\pi}{N_T}q}. \tag{14.73}
$$

In practice one calculates $\hat{E}_z^k(m,n)$ and the spectral representation of the magnetic fields in the same way, i.e., as in (14.71). Then one multiplies $\hat{E}_z^k(m,n)$ by $\exp(-jk\pi/N_T)$ to account for the temporal offset.

The spatial offset is slightly more problematic than the temporal offset. As shown in Fig. 14.4, the integration boundary can be aligned with only one of the fields. The magnetic field tangential to the integration boundary is found from the nodes that are a spatial half-step to either side of the boundary.

To obtain the magnetic field on the boundary, the traditional approach has been to use a spatial average of the nodes to either side of the boundary. For example, along the right side of the boundary, the harmonic magnetic field would be given by

$$
\hat{H}_y^k(m,n) = \frac{1}{2}\mathcal{F}\left[H_y^{q-1/2}(m-1,n) + H_y^{q-1/2}(m,n)\right]. \tag{14.74}
$$

Because of this spatial average, $\hat{H}_y(m, n)$ and $\hat{E}_z(m, n)$ are assumed to be collocated and, with the temporal phase correction, can be used to determine the equivalent currents over the integration boundary (which are then used in the NTFF transform itself).

Unfortunately the arithmetic mean used in (14.74) introduces errors. To illustrate this, assume a harmonic plane wave is propagating in the grid. The temporal frequency ω is $2\pi k'/N_T$ where k' is an integer constant and, as before, N_T is the total number of time-steps in a simulation. The y component of the magnetic field is given by

$$H_y^{q-1/2}(m, n) = \cos\left(\omega\left[q - \frac{1}{2}\right]\Delta_t - \xi\right) \tag{14.75}$$

$$= \frac{e^{j\left(k'\frac{2\pi}{N_T}[q-\frac{1}{2}]\Delta_t+\xi\right)} + e^{-j\left(k'\frac{2\pi}{N_T}[q-\frac{1}{2}]\Delta_t+\xi\right)}}{2}, \tag{14.76}$$

where $\xi = \beta_x(m + 1/2)\Delta_x + \beta_y n\Delta_y$, and β_x and β_y are the x and y components of the wave vector, respectively. Taking the discrete Fourier transform of (14.76), i.e.,

$$\hat{H}_y^k(m, n) = \frac{1}{N_T} \sum_{q=\langle N_T\rangle} H_y^{q-1/2}(m, n)e^{-jk\frac{2\pi}{N_T}\left(q-\frac{1}{2}\right)}, \tag{14.77}$$

one notes that the sum yields zero when k is anything other than k' or $N_T - k'$. The values of k that yield non-zero correspond to the positive and negative frequency of the continuous world and, like the continuous world, the corresponding spectral values are complex conjugates. Without loss of generality, we will continue the discussion in terms of the spectral component corresponding to the positive frequency, i.e.,

$$\hat{H}_y^{k'}(m, n) = \frac{1}{2} \exp(-j[\beta_x(m + 1/2)\Delta_x + \beta_y n\Delta_y]). \tag{14.78}$$

(Note that since the time-domain functions are real-valued, in practice one does not need to calculate the transform at any of the negative frequencies. They are merely the complex conjugates of the values at the positive frequencies.)

Because the Fourier transform is a linear operator, using (14.76) in (14.74) yields

$$\hat{H}_y^{k'}(m, n) = e^{-j\beta_y n\Delta_y}\frac{e^{-j\beta_x\left(m-\frac{1}{2}\right)\Delta_x} + e^{-j\beta_x\left(m+\frac{1}{2}\right)\Delta_x}}{4}, \tag{14.79}$$

$$= \frac{1}{2}e^{-j(\beta_x m\Delta_x+\beta_y n\Delta_y)}\cos\left(\frac{\beta_x\Delta_x}{2}\right). \tag{14.80}$$

The exact expression for the magnetic field on the integration boundary is $\exp(-j[\beta_x m\Delta_x + \beta_y n\Delta_y])/2$. Thus, the cosine term represents an error—one which vanishes only in the limit as the spatial-step size goes to zero.

Instead of taking the Fourier transform of the average of the time-domain fields, let us take the Fourier transform of the fields to either side of the boundary. We define the transforms as

$$\hat{H}_y^+(m, n) = \mathcal{F}\left[H_y^{q-1/2}(m, n)\right], \tag{14.81}$$

$$\hat{H}_y^-(m, n) = \mathcal{F}\left[H_y^{q-1/2}(m - 1, n)\right]. \tag{14.82}$$

Still assuming a single harmonic plane wave, for the "positive frequency" corresponding to $k = k'$, $\hat{H}_y^+(m,n)$ and $\hat{H}_y^-(m,n)$ are given by

$$\hat{H}_y^+(m,n) = \frac{1}{2} e^{-j(\beta_x(m+1/2)\Delta_x + \beta_y n \Delta_y)}, \tag{14.83}$$

$$\hat{H}_y^-(m,n) = \frac{1}{2} e^{-j(\beta_x(m-1/2)\Delta_x + \beta_y n \Delta_y)}. \tag{14.84}$$

Were one to calculate the arithmetic mean of $\hat{H}_y^+(m,n)$ and $\hat{H}_y^-(m,n)$, the result would be the same as given in (14.80). However, consider the geometric mean (where the geometric mean of a and b is $\sqrt{ab}$) of $\hat{H}_y^+(m,n)$ and $\hat{H}_y^-(m,n)$:

$$\hat{H}_y^{k'}(m,n) = \left(\hat{H}_y^+(m,n) \hat{H}_y^-(m,n) \right)^{1/2}, \tag{14.85}$$

$$= \frac{1}{2} e^{-j(\beta_x m \Delta_x + \beta_y n \Delta_y)}. \tag{14.86}$$

This is precisely the correct answer. There is no error introduced by the geometric mean. A note of caution: when calculating the square root of these complex quantities, one must ensure that the proper branch cut is selected. Thus, when $\hat{H}_y^+(m,n)$ and $\hat{H}_y^-(m,n)$ have phases near $\pm\pi$ the geometric mean should also have a phase near $\pm\pi$ rather than near zero.

In practice, at any given frequency there will be an angular spectrum of wave vectors present and hence any averaging, whether geometric or arithmetic, will introduce some errors. However, for a single wave vector the geometric mean is exact and it has been our experience that the geometric mean provides superior results for nearly all discretizations and scattering angles. The following section demonstration the use of the geometric mean in several scenarios.

14.7 NTFF Transformations Using the Geometric Mean

14.7.1 Double-Slit Radiation

To demonstrate the difference between the arithmetic and geometric mean, we begin by considering the radiation from a double-slit aperture in a perfect electrical-conductor (PEC) screen which is illuminated by a normally incident pulsed plane wave. TM^z polarization is assumed. As shown in Fig. 14.5(a), in this case the boundary over which the fields are measured is three-sided and exists on only one side of the screen.

Given the fields over the three-sided boundary, one then assumes the fields "interior" to this boundary (i.e., the region which includes the slits) are zero while the fields exterior to the boundary are unchanged. To account for the discontinuity in the fields across the integration boundary, surface currents must be present. Since the fields are zero within the boundary, one can replace the actual interior with anything without affecting the exterior fields. One thus assumes that the slits are not present—that the PEC plane is unbroken. The surface currents over the three-sided boundary are now radiating in the presence of an infinite plane. The far-field radiation can be calculated with a three-sided integral where one uses the Green's function for a source above an infinite plane. This, equivalently, from image theory, is simply the radiation from the original (measured) current and the image of the current. Both the measured current and the image current are radiating in free

space. In this way the three-sided boundary can be replaced with a closed four-sided boundary as shown in Fig. 14.5(b). The corresponding currents over this surface, i.e., the measured currents over half the boundary and the image currents over the other half, are transformed to the far field.

The incident field is introduced over a total-field/scattered-field (TFSF) boundary which only exists to the left side of the screen. The grid is terminated with an eight-cell perfectly matched layer (PML).

The right side of the integration surface is D cells away from the PEC screen. The length of the right side of the integration boundary is held fixed at 75 cells. In principle, the location of the integration boundary should make no difference to the far-fields. However, when using the arithmetic mean, the far-fields are sensitive to the boundary location, i.e., sensitive to the value of D. Note that were a single component of the field integrated over the aperture, as advocated by [1], averaging is not an issue. However, that approach is restricted to screens which are planar and there are no inhomogeneities present other than the screen. The approach we advocate can accommodate any screen or scatterer geometry provided it can be contained within the integration boundary. Nevertheless, we will employ the aperture-based approach as a reference solution.

The simulation uses "slits" which are 15 cells wide. The PEC between the slits is 30 cells wide. The excitation is a Ricker wavelet discretized such that there are 30 cells per wavelength at the most energetic frequency. The simulation is run at the 2D Courant limit $(1/\sqrt{2})$ for 1024 time steps.

Figure 14.6(a) shows the far-field radiation pattern which is obtained using the arithmetic mean. The pattern is symmetric about zero degrees which corresponds to the direction normal to the screen. The radiation pattern is calculated using

$$\frac{1}{\lambda} \lim_{\rho \to \infty} \left[2\pi\rho \frac{|\hat{E}_z(\phi)|^2}{|\hat{E}_z^i|^2} \right] \tag{14.87}$$

where ϕ is the scattering angle, ρ is the distance from the slits, $\hat{E}_z(\phi)$ is the field radiated in the ϕ direction, and $\hat{E}_z^i$ is the complex amplitude of the incident plane wave at the frequency of interest. Results are shown for a frequency corresponding to 10.0566 cells per wavelength. Figure 14.6(a) shows the pattern when D is either 5, 6, or 7 cells.

Note that there are significant differences in the central peak depending on the displacement D between the right-side integration boundary and the PEC screen. Figure 14.6(b) shows an expanded view of the pattern in the neighborhood of the peak. As can be seen, displacing the integration boundary by two cells causes a change in the peak of approximately 9 percent. The results as a function of displacement are nearly periodic, e.g., displacements of 5 and 15 cells (not shown) yield nearly the same results as do displacements of 6 and 16 cells, and so on. (The period of 10 cells is a consequence of examining a frequency corresponding to approximately 10 cells per wavelength.) Also shown as plus signs in Fig. 14.6(b) are the results obtained when the transform uses the electric field (i.e., the equivalent magnetic current) over the aperture. No averaging is involved in this case. The aperture-based results are seen to agree well with the arithmetic-mean results when the displacement D is 5 cells. Unfortunately one does not know *a priori* that this agreement will exist nor does this displacement provide similar agreement for other frequencies.

On the other hand, when using the geometric mean, there is almost no variation in the radiation pattern as the integration boundary is displaced. Figure 14.6(c) shows the same results as presented in Fig. 14.6(b) except now the geometric mean of the harmonic fields is used to obtain the magnetic
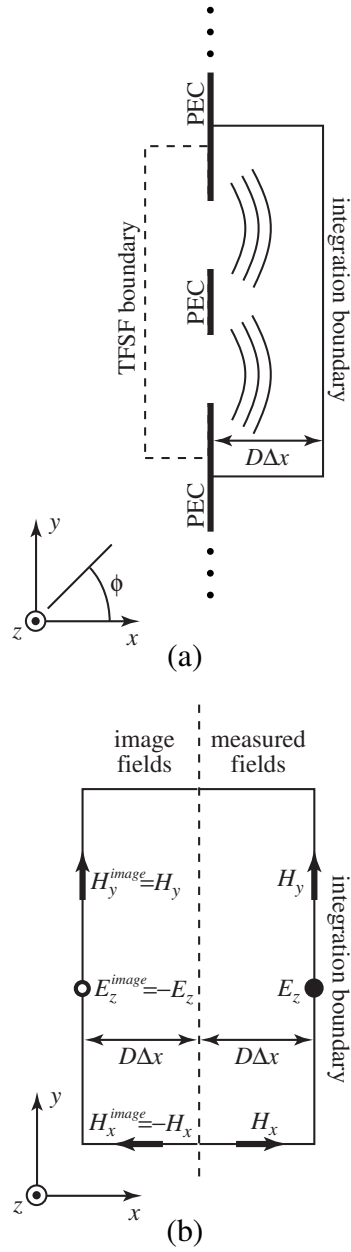
Figure 14.5: (a) Geometry of the double-slit experiment. A pulsed plane wave is introduced via a TFSF boundary on the left side of the screen. The field are recorded over the three-sided integration boundary to the left of the screen. (b) Image theory is used to create a four-sided closed surface over which the currents are transformed to the far-field. The dashed line corresponds to the location where the PEC plane had been.
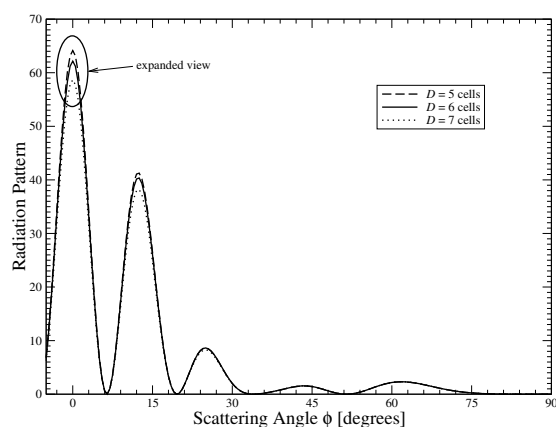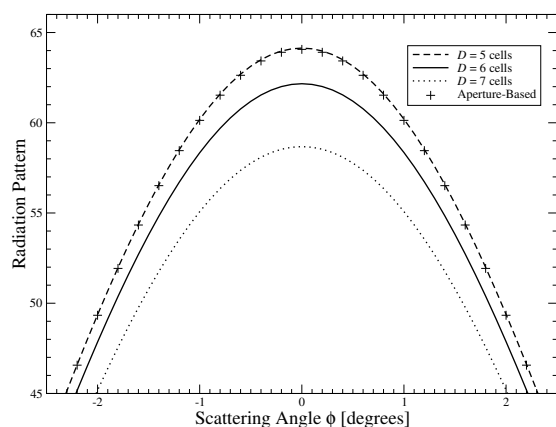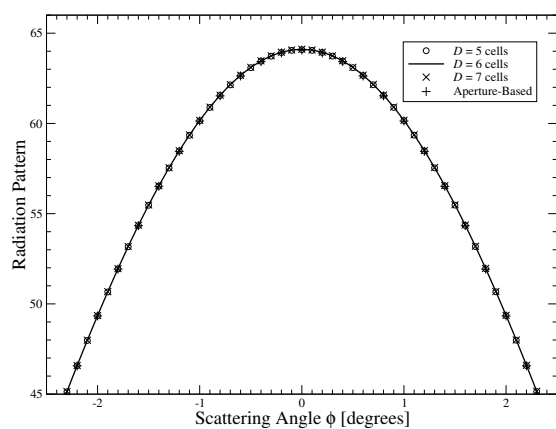
Figure 14.6: (a) Radiation from the double slit for angles between -5 and 90 degrees (the pattern is symmetric about zero degrees). Results are shown for boundary displacements D of 5, 6, and 7 cells. The arithmetic mean is used. (b) Expanded view of the central peak using the arithmetic mean. Also shown are the fields obtained when a single field component is recorded over the aperture and transformed to the far field. (c) Same as (b) except the geometric mean is used. The variation of the fields caused by the displacement of the boundary is now essentially negligible.
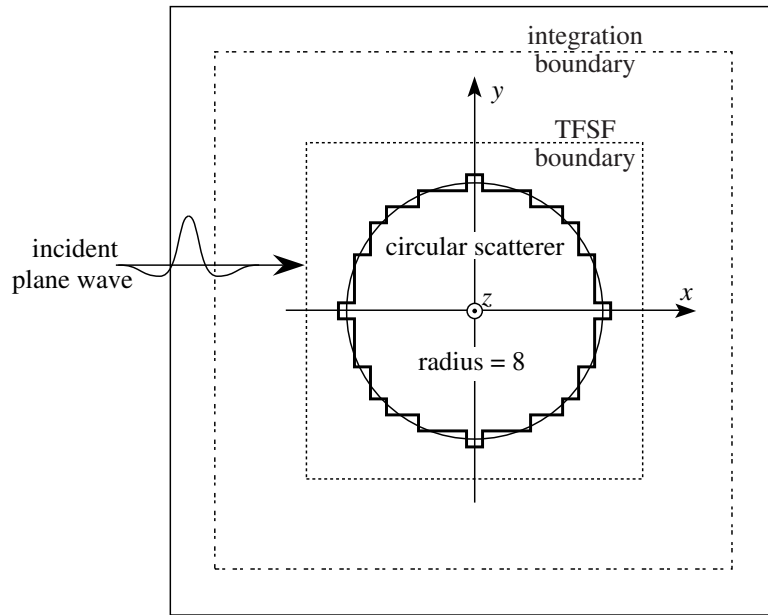
Figure 14.7: Geometry of the circular PEC cylinder.

fields on the integration boundary. The variation between these peaks is less than 0.022, i.e., a reduction in variation by a factor of approximately 270. This demonstrates that, unlike with the arithmetic mean, the location of the integration boundary is effectively irrelevant when using the GM-NTFF transform.

Naturally, at finer discretizations, the difference between the geometric mean and the arithmetic mean are less dramatic, but the geometric mean consistently performs better than the arithmetic mean.

(Simpson's rule was used for all integrations except for the integration of the aperture fields where a Riemann sum was used.)

14.7.2   Scattering from a Circular Cylinder

Consider scattering from a PEC circular cylinder under TM^z polarization as shown in Fig. 14.7. The Dey-Mittra scheme is employed to help reduce the effects of staircasing [2]. The cylinder has eight cells along its radius. A pulsed plane wave which travels in the x direction is introduced via a TFSF boundary. The simulation is run 512 time steps. Because the Dey-Mittra scheme is used, the Courant number was reduced to approximately 35 percent of the 2D limit in order to ensure stability [3].

Figure 14.8 shows the wavelength-normalized scattering width of the cylinder as a function of scattering angle obtained using the series solution for a circular cylinder [4], the arithmetic-mean NTFF transform, and the GM-NTFF transform. (The normalized scattering width is the same as the radiation pattern given in (14.87) where ρ is now taken to be the distance from the center of the cylinder.) The discretization is such that there are 9.92526 cells per wavelength at the frequency being considered here. One should keep in mind that the discretization of the cylinder introduces some errors and hence the "exact" solution for a circular cylinder is not truly exact for the scatterer
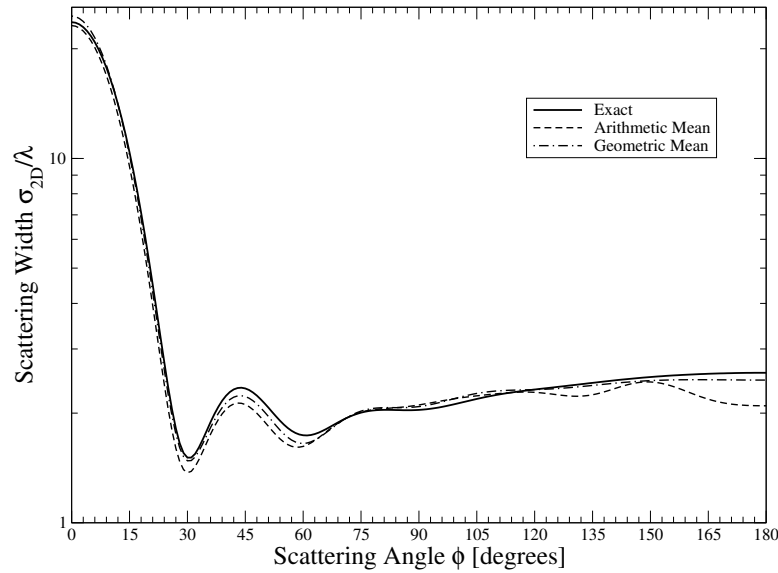
Figure 14.8: Scattering width of a circular cylinder. The radius is eight cells and the frequency corresponds to 9.92526 cells per wavelength.

present in the simulation. Therefore, the reference solution does not provide a perfect way with which to judge the solutions. Nevertheless, one hopes that the FDTD scatterer, when employing the Dey-Mittra scheme, is a close approximation to a true circular scatterer and thus the exact solution from the continuous world provides a reasonable basis for comparison.

The difference between the solutions in Fig. 14.8 are seen to be relatively small. Figure 14.9 shows a plot of the magnitude of the difference between the exact solution and the FDTD-based solutions. Although there are angles where the arithmetic mean performs better than the geometric mean, in general the geometric mean is better. The integrated error for angles between 0 and π is 0.6936 for the arithmetic mean and 0.3221, i.e., the error is reduced by more than a factor of two by using the geometric mean.

14.7.3   Scattering from a Strongly Forward-Scattering Sphere

Finally, consider scattering from a dielectric sphere, depicted in Fig. 14.10, which has a relative permittivity ϵ_r of 1.21. Such a sphere was considered in [5] and can also be found in Sec. 8.7 of [6]. In this case the transformation traditionally entails finding the tangential fields over the six sides of a cuboid which bounds the sphere. The sphere is discretized such that there are 60 cells along the radius. A staircase representation is used (where a node is simply either inside or outside the sphere). The simulation is run at 95 percent of the 3D Courant limit ($0.95/\sqrt{3}$) for 2048 time steps. The grid is terminated with an eight-cell perfectly-matched layer.

Figure 14.11 shows the normalized scattering cross section as a function of the equatorial angle ϕ. The frequency corresponds to 20.06 cells per wavelength. The exact solution was obtained via the Mie series (see, e.g., [7]). As was the case in 2D, both the arithmetic and geometric mean perform reasonably well, but the geometric mean is generally more accurate than the arithmetic mean. In Fig. 14.11 visible errors are only present near the back-scattering direction of $\phi = 180$
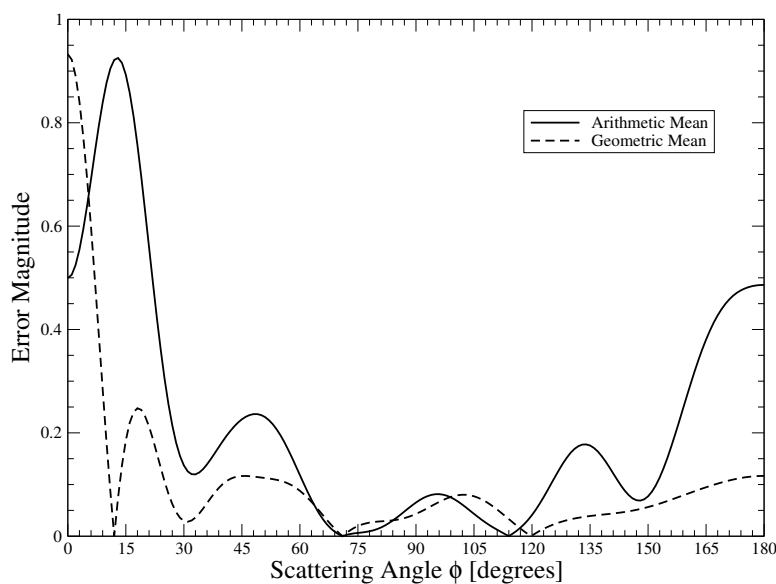
Figure 14.9: Magnitude of the difference between the FDTD-based solutions and the nominally exact solution.
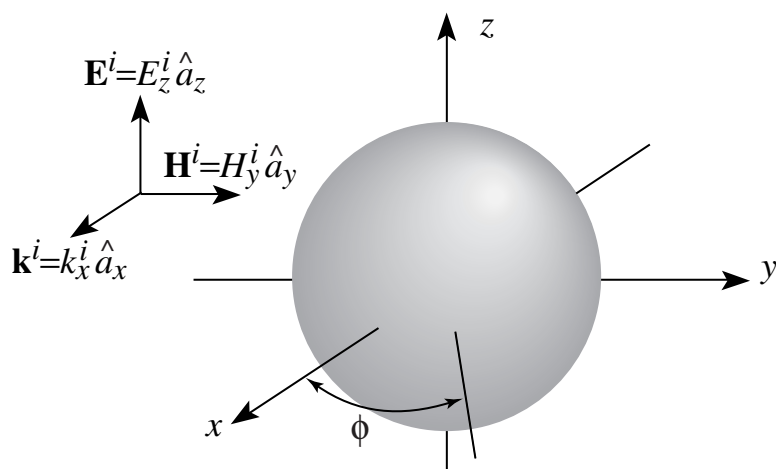

Figure 14.10: Geometry of the dielectric sphere. The relative permittivity ϵ_r is 1.21. This incident field is polarized in the z direction and travels in the x direction. The equatorial angle ϕ is in the xy-plane with $\phi = 0$ corresponding to the $+x$ direction.
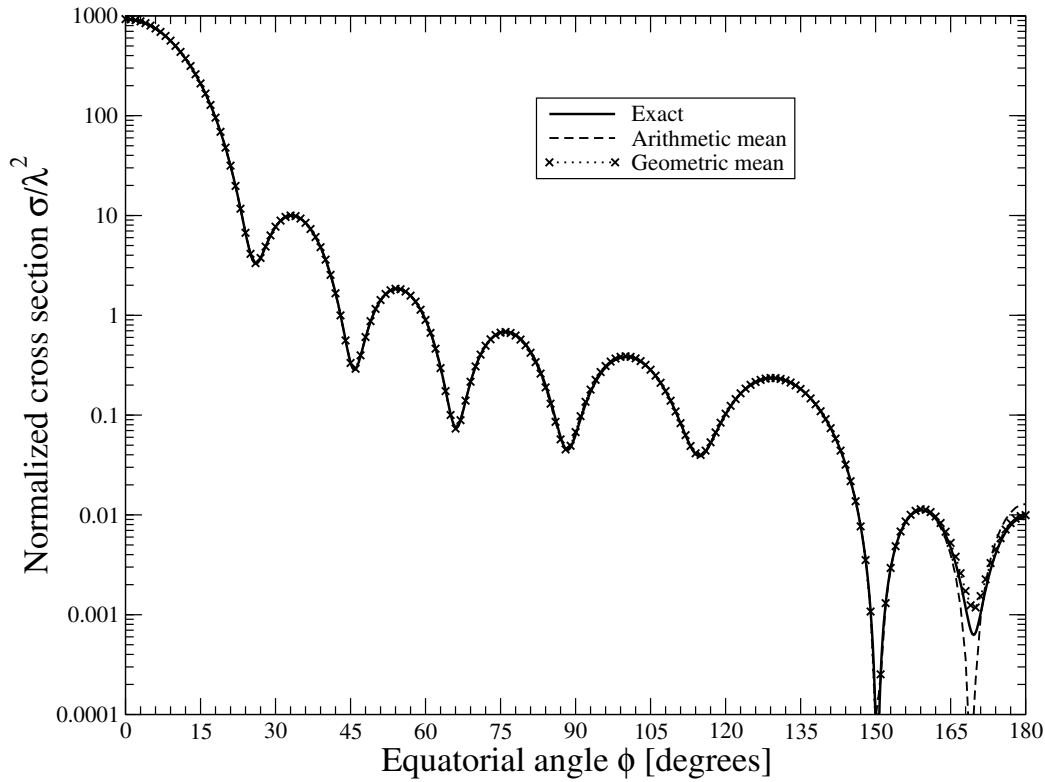
Figure 14.11: Scattering cross section of a dielectric sphere versus the equatorial angle ϕ. The sphere is discretized with 60 cells along the radius and the frequency used here corresponds to 20.06 cells per wavelength.

degrees. Note that there is a large difference, approximately five orders of magnitude, between the scattering in the forward and backward directions.

In order to improve the results in the back-scattering direction Li *et al.* [5] advocated calculating the transformation using the five faces other than the forward-scattering face. Figure 14.12 shows the normalized backscattering cross section versus wavelength (expressed in terms of number of cells per wavelength) calculated using the arithmetic mean. The normalized cross section is given by

$$\frac{1}{\lambda^2} \lim_{r \to \infty} \left[4\pi r^2 \frac{|\hat{E}_z(\theta, \phi)|^2}{|\hat{E}_z^i|^2} \right] \tag{14.88}$$

where r is the distance from the center of the sphere, θ is the azimuthal angle and ϕ is the equatorial angle. For backscatter, θ is $\pi/2$ and ϕ is π.

The NTFF transform results shown in Fig. 14.12 were calculated using either the fields over all six faces of the integration boundary or the fields over the five faces advocated by Li *et al.* The results in this figure correspond to those shown in Fig. 1(b) of [5] for the sphere with a radius of 3 μm. (However, for the sake of generality, here the results are plotted in terms of unitless quantities.) Note that the six-sided arithmetic-mean results presented here are better than those presented in [5]. We were able to duplicate the results presented in [5] by not applying a temporal phase-correction factor (or, similarly, by applying a correction factor which is twice the factor given here). Nevertheless, the recommendation of Li *et al.* is true that the five-sided computation
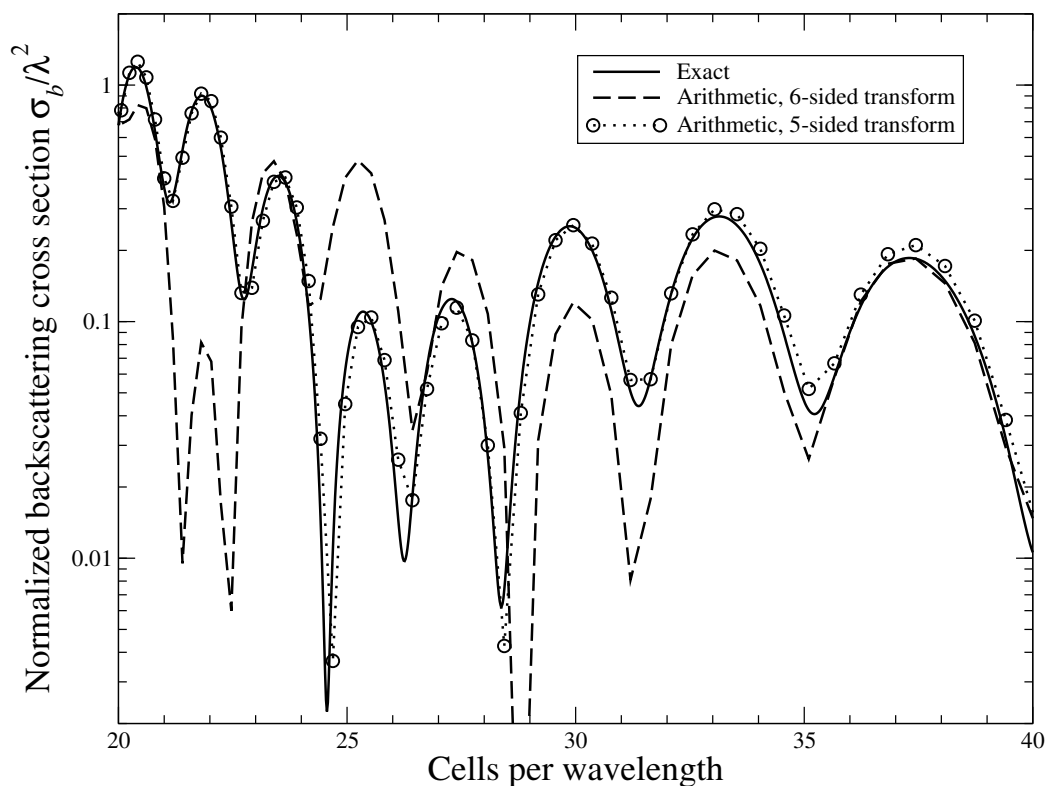
Figure 14.12: Backscatter from a sphere with $\epsilon_r = 1.21$ versus the wavelength (expressed in terms of number of cells). The FDTD transformations are calculated using the arithmetic mean and either a five- or six-sided transformation boundary.

is better than the six-sided one for calculating the backscattering when using the arithmetic mean. However, for directions other than backscatter or for other sizes, one does not know *a priori* if a face should or should not be discarded.

Figure 14.13 is the same as Fig. 14.12 except the transformation is done using the GM-NTFF transform. In this case discarding data from the forward-scattering face actually slightly degrades the quality of the transform. Thus, when using the geometric mean there is no need to discard data. One can use it confidently for all scattering angles and all sizes.

To summarize, unlike the traditional arithmetic mean, for a single harmonic plane wave the geometric mean accounts for the spatial offset of the fields in a way that is exact. In practice, where a spectrum of wave vectors are present, the geometric mean typically performs significantly better than the arithmetic mean. The geometric mean is much less sensitive to the integration-boundary location than is the arithmetic mean. For strongly forward-scattering objects, the use of the geometric mean obviates the need to discard the fields over the forward face (as has been advocated previously) when calculating the backscatter. The geometric mean does entail a slight increase in computational cost because for each node along the integration boundary a DFT must be calculated for three fields instead of two. However, this cost is typically minor compared to the overall simulation cost.
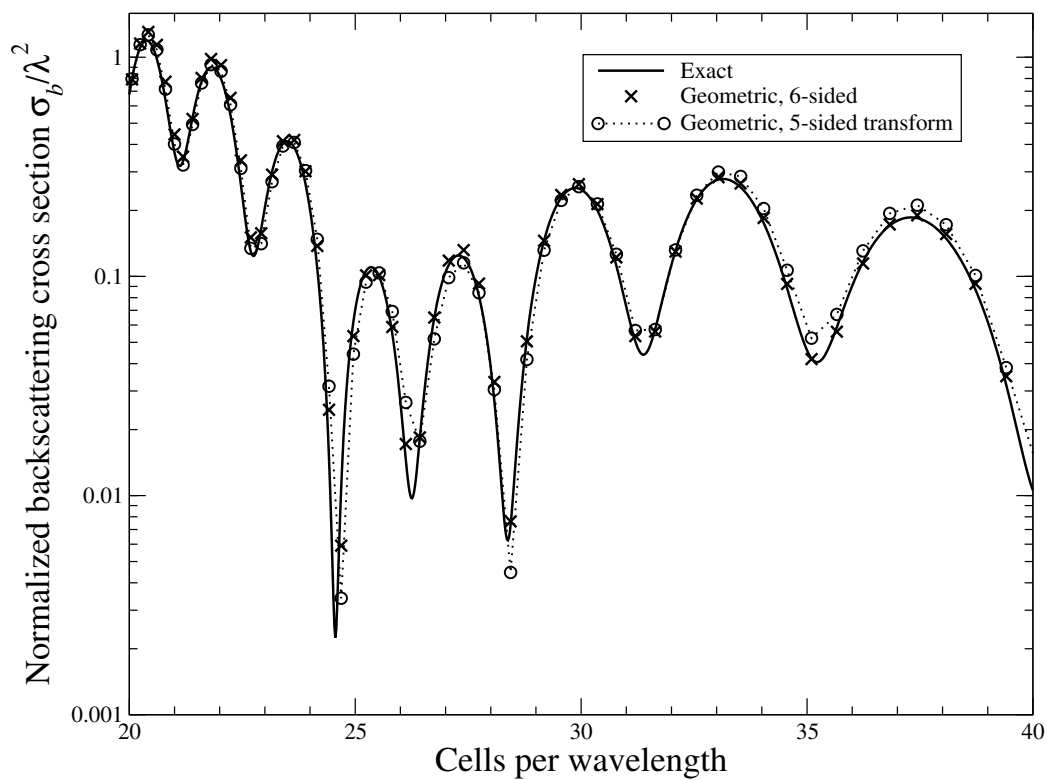
Figure 14.13: Backscatter from a sphere with $\epsilon_r = 1.21$ versus the wavelength (expressed in terms of number of cells). The transformations use the geometric mean and the fields over either five or six faces of the integration boundary.